Nanoscale

PAPER

View Article Online
View Journal | View Issue

Cite this: *Nanoscale*, 2024, **16**, 22240

Bifunctional electrocatalytic hybrid heterostructures for polysulfide anchoring/conversion for a stable lithium–sulfur battery†

Sakthivel Kaliyaperumal,[a] Karthik Kiran Sarigamala,*[a] Padmini Moorthy,[b] Balaji Ramachandran,[c] Narendhar Chandrasekar[d] and Tim Albrecht[e]

Received 2nd August 2024,
Accepted 29th October 2024

DOI: 10.1039/d4nr03190c

rsc.li/nanoscale

In situ phase engineering of transition metal dichalcogenides (TMDs) with controlled sulfur vacancies offers a promising strategy for superior-performance lithium–sulfur (Li–S) batteries. Herein, we demonstrate a bifunctional approach by designing a sulfur host material using 1T-MoS_2/MoO_3 heterostructures grown directly on carbon nanopot-resembling designer structures (CMS). The metallic phase (1T-MoS_2) with MoO_3 synergistically contributes to exceptional electronic transport, increased interlayer spacing, and more electrochemically active sites across its basal plane. Carbon nanopot structures and sulfur vacancies within the TMDs act as anchoring sites for lithium polysulfides (LiPSs). Additionally, the specifically phase-engineered 2D heterostructure promotes their efficient conversion into the electrochemically favorable Li_2S phase. This dual functionality is expected to significantly improve the rate capability and cycle life stability of Li–S batteries. This translates to a high reversible rate capacity of 1205 mA h g^{-1} at a current density of 0.2 A g^{-1}. The sulfur-loaded CMS nanostructure shows an excellent cycling life with a decay rate of only 0.078% over 1100 cycles at 1 A g^{-1}, underscoring the effectiveness of the *in situ* phase engineering approach for creating a stable Li–S battery.

1 Introduction

Two-dimensional (2D) materials research has seen significant growth from the past few decades owing to their unique properties and potential applications.[1,2] Molybdenum disulfide (MoS_2), a widely studied layered 2D material, exhibits fascinating electronic and optical properties that are dependent on its layer count.[3,4] However, researchers are constantly seeking new ways to expand the functionalities of MoS_2 by designing novel interfacial architectures.[5] Conventional heterostructure fabrication often relies on the physical stacking of different 2D nanomaterials *via* van der Waals forces. However, such methods can be challenging for precise synthesis.[6] In this context, the chemical transformation of 2D materials offers a promising approach for engineering novel architectures with tailored properties by directly converting the layers of a supported 2D material into a new material with a different chemical composition, all while keeping it on the same template. By carefully selecting reaction conditions, conversion across basal planes can be controlled.[7,8] This level of control is crucial for maintaining the desired properties and functionality of the resulting heterostructure. Furthermore, their geometric alignment, electronic structure, and chemical reactivity provide valuable insights into their fundamental behavior, leading to interesting phenomena specific to their low-dimensional nature.[9] On-stack *in situ* phase transformation enables layer-by-layer control of the heterostructure, offering superiority over traditional doping methods, thermal evaporation, and sputter deposition routes.[10–13] Localized *in situ* transformation within an MoS_2 template leads to the coexistence of MoS_2 and MoO_3 phases with large-scale homogeneity, exemplifying the creation of a multifunctional material with tuneable properties. Sheehan *et al.* studied this concept through atomic force microscopy (AFM) and understood that frictional anisotropy on single crystal MoS_2 induces the atomic sliding of MoO_3 nanocrystals.[14] Yoon *et al.* reported that thermal treatment of MoS_2 at ~400 °C triggers oxidation of the sample into layered α-MoO_3 nanosheets, epitaxially stacking them on the MoS_2 surface through van der Waals forces, with six possible orientations.[15] It can also be realized that the interconversion

---

[a] CO_2 Research and Green Technologies Centre, Vellore Institute of Technology, Vellore, Tamil Nadu, 632014, India. E-mail: karthikkiran.sarigamala@vit.ac.in
[b] Department of Green Energy Technology, Pondicherry University, 605014, India
[c] Department of Electronics and Communication Engineering, Centre of Excellence for Nanotechnology, Koneru Lakshmaiah Education Foundation, Andhra Pradesh – 522302, India
[d] Department of BioNano Technology, Gachon University, Republic of Korea
[e] School of Chemistry, University of Birmingham, Birmingham, B15 2TT, UK

† Electronic supplementary information (ESI) available. See DOI: https://doi.org/10.1039/d4nr03190c

mechanism between MoS_2 and MoO_3 offers a platform for interfacial transformation through either oxidation or reduction.[16,17] This approach can leverage a key advantage, such as utilizing high-quality conductive 1T MoS_2 layers as starting materials grown using interfacial engineering techniques. This choice of starting phase ensures a truly multifunctional material, a conductive hetero-phase stack where the initial 1T MoS_2 layer remains and integrates with the subsequently formed MoO_3 phase.[18,19] Currently, these attractive heterojunction materials formed from the *in situ* phase transformation are actively finding applications in Li–S batteries. Lei *et al.* explored MoS_2–MoO_3 nanosheets as active catalysts to improve the polysulfide conversion reactions, achieving a specific capacity of 1531 mA h g^{-1} at 0.2C rate.[20] Yang *et al.* prepared the MoO_3/MoS_2 flexible paper as a sulfur host and polysulfide conversion accelerator, achieving 911.3 mA h g^{-1} at a low C-rate of 0.1C after 500 cycles.[21] In general, the intrinsic kinetics of sulfur redox reactions in Li–S batteries are governed by the solvation chemistry.[22,23] Enhancing the electrocatalytic activity through kinetic promoters such as homogeneous, heterogeneous, and semi-immobilized systems helps reduce the accumulation of lithium polysulfides (LiPS) in the electrolyte, thereby improving the overall performance of Li–S batteries.[24,25]

Additionally, advanced catalytic nanostructures, such as hollow carbon-templated MoS_2-based supports, play a crucial role in trapping and converting LiPS intermediates formed during discharge.[26–28] This approach significantly mitigates the detrimental shuttle effect, further enhancing the battery efficiency and cycle stability. Thus, on-stack transformations of the MoS_2 layers on the designer carbon nanosupport with a hollow interior or porous structures provide a superior platform for the growth and dispersion of active materials like MoS_2 and MoO_3,[29,30] which translates to a higher capacity.[31,32]

In this work, we have developed an intricate hybrid heterostructure as a bifunctional catalytic host material for Li–S battery cathodes. Through strategic growth of a low-dimensional MoS_2/MoO_3 heterostructure on hard carbon templates, such as hollow carbon nanopots, we achieved the desired morphologies. This was facilitated by a controlled chemical and thermal environment, enabling *in situ* phase transformation. The hierarchical structure helps to host a large quantity of sulfur through its porous structure, and also serves as a functional catalyst to trap and convert polysulfide. The three-dimensional (3D) radial assembly of the heterostructure layers on carbon templates further enhances the Li–S battery performance by promoting the active site distribution and facilitating the rapid lithium-ion movement. The resultant hierarchical cathode shows an impressive rate capability with the highest specific capacity of 1205 mA h g^{-1} at 0.2 A g^{-1}, and holds a reversible specific capacity of 1106 mA h g^{-1} even after 200 cycles (coulombic efficiency of more than 99%) at 0.2 A g^{-1}. An outstanding specific capacity of ~834 mA h g^{-1} at 1 A g^{-1} is retained after a long-term stability test (only 0.078% decay in capacity/cycle) over 1100 cycles. Thus, the synergistic design approach holds promise for developing next-generation Li–S battery electrodes with improved performance.

2. Experimental

2.1 Synthesis of 1T-MoS_2/C

100 mg of C-nanopots, 10 mmol of ammonium molybdate heptahydrate, and 0.5 mol of thiourea were added to 50 mL of deionized water, and stirred to obtain a homogeneous solution (Experimental procedures on C-nanopot are provided in ESI SI-1.1†). Then, the homogeneous suspension was transferred to a 100 mL volume Teflon-lined autoclave, and the temperature was maintained at 180 °C for a duration of 24 hours. The final product was meticulously cleaned with Millipore water and ethanol. Later, the sample was dried at 80 °C overnight in a vacuum oven, and the samples were labeled as 1T-MoS_2/C.

2.2 Synthesis of CMS

In the next stage, the 1T-MoS_2/C powder was sonicated in 3% H_2O_2 to undergo mild oxidation, and then the sample was transferred into a tubular furnace. The furnace temperature was set to 350 °C at a ramp rate of 5 °C min^{-1} under Ar (95%) + H_2 (5%) gas flow. After three hours of reaction time, the final product was collected and labeled as CMS.

3. Results and discussion

3.1 Microstructural, morphological, and composition analysis

Fig. 1(a) shows the pyrolyzed carbon nanostructures that bear a resemblance to traditional handmade pottery (C-nanopots). Initially, the self-directed growth of 1T-MoS_2/C was synthesized through an *in situ* hydrothermal growth methodology, as illustrated in Fig. 1(a)-left panel. X-ray diffraction analysis (XRD) was carried out to investigate the microstructural features of the prepared specimens. The XRD patterns (Fig. 1(a)-right panel) reveal a broad, amorphous peak corresponding to C-nanopots, and the MoS_2/C exhibits suboptimal crystallinity characterized by an enlarged interlayer spacing, which is possibly due to the relatively modest growth temperature employed. Expressly, 1T MoS_2/C in Fig. 1(a)-right panel shows a prominent diffraction peak at $2\theta = 9.31°$ which signifies an increased *d*-spacing between the interplanar planes of 9.48 Å, in contrast to the conventional 2H phase MoS_2 sample with a *d*-spacing of merely 6.15 Å.[33,34] Moreover, a diffraction peak of second order related to the (004) plane was observed at approximately 18.43°. Second-order diffraction peaks, such as the (004) peak for 1T MoS_2, appear at approximately double the 2θ angle of the first-order (002) peak, offering insights into the material's periodicity and layer stacking. These peaks confirm the crystal's periodic structure, and serve as indicators of the synthesis quality and uniformity.[35] First-order peaks, like the (002) reflection, occur at lower angles and provide information about the fundamental interlayer spacings. Together, these

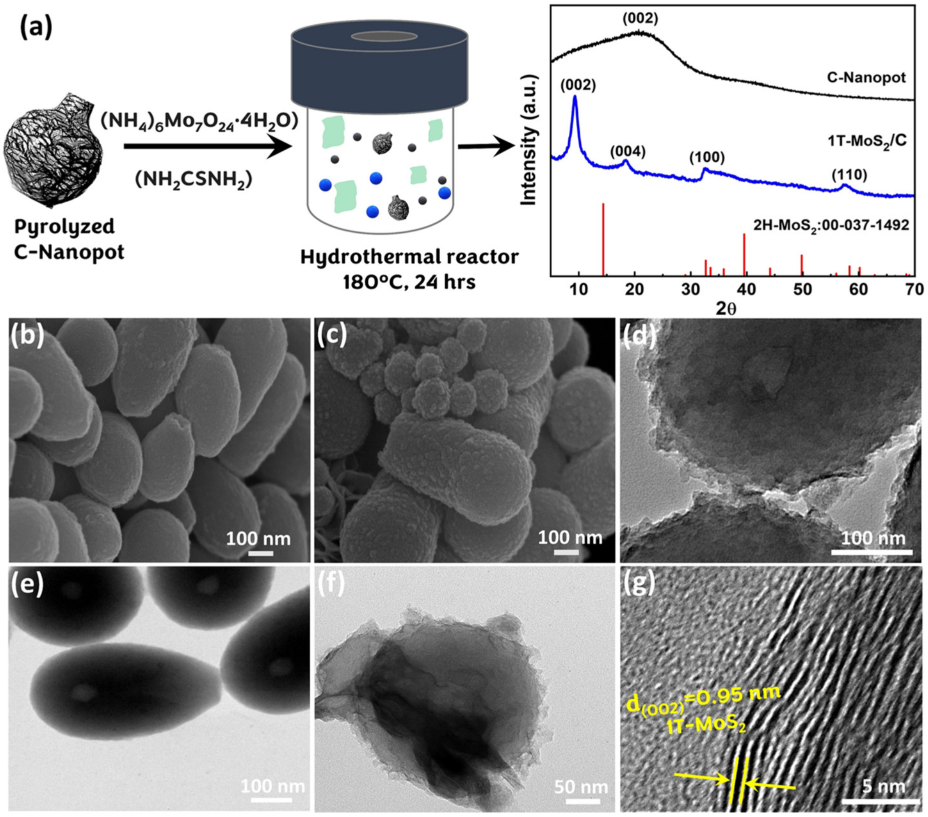

Fig. 1 (a) Schematic showing the synthesis of 1T MoS_2 on carbon nanopots (1T MoS_2/C) (left panel) and XRD (right panel); (b and e) SEM and TEM micrographs of the pyrolyzed carbon nanopots, respectively; (c) SEM of 1T MoS_2/C; (d and f)-TEM of 1T MoS_2/C; (g) high-resolution TEM image showing diffraction fringes of 1T MoS_2.

peaks are essential for assessing the crystallinity, interlayer spacing, and overall quality of the synthesized 1T MoS_2.[36] The difference in the $d_{(002)}$ spacing of 1T MoS_2/C and 2H-MoS_2, which is approximately 3.33 Å, aligns with the hydrogen-bonding diameter of ammonium ions (≈3.5 Å) in metal disulfides, underscoring the strong stability associated with the intercalation of ammonium ions.

The scanning electron microscope (SEM) and transmission electron microscope (TEM) images in Fig. 1(b) and (e) reveal the uniformly distributed carbon templates with hollow interiors resembling the pot morphology. Fig. 1(c) and (f) show the growth of ultra-thin 1T-MoS_2 sheets on the surface of the hard templates (C-nanopots). The magnified image in Fig. 1(d) reveals the interface, where the MoS_2 nanosheets appear to wrap completely around the carbon template. The curly texture of the nanosheets suggests they are both flexible and very thin. Finally, the high-resolution TEM image (HR-TEM) in Fig. 1(g) displays the diffraction patterns of these 1T-phase nanosheets. The spacing between atomic planes, ranging from ~0.93 nm to 0.95 nm, matches the (002) plane observed in the XRD analysis.

In the subsequent stage, 1T-MoS_2/C (Fig. 2(a)) is used to prepare MoS_2/MoO_3 heterostructures through a phase transition. This material is subjected to mild oxidation with 3% H_2O_2, likely introducing defects in the MoS_2 structure (vacancies/interstitials, dislocations) and transformation of the specimen to MoO_3, forming an interfacial stack. The overall phase transition can be represented by the reaction:

$$MoS_2 + H_2O_2 + H_2O \rightarrow MoO_3 + 2H_2S.$$

Subsequent calcination at 350 °C in an inert atmosphere further promotes sulfur vacancies by providing enough energy for some sulfur atoms to escape the MoS_2 lattice. This vacancy creation disrupts the crystal structure. The final product (CMS) is a mixed-phase material with dominant 1T-MoS_2 and MoO_3. The phase transition can also induce a partial conversion of 1T-MoS_2 to the 2H-MoS_2 phase. SEM and TEM images in Fig. 2(b) and (c) confirm the uniform formation of a hierarchical hybrid structure. A hollow carbon nanopot serves as the core template encapsulated by radially aligned MoS_2/MoO_3 nanosheets. The scanning transmission electron microscopic (STEM) image reveals the hollow morphology of the carbon core radially encapsulated by MoS_2/MoO_3 nanosheets after the pyrolysis process, Fig. 2(d).

The high resolution-TEM (HR-TEM) image (Fig. 2(e)) reveals the characteristic interlayer spacing (~0.94 nm) for 1T-MoS_2, and a lattice spacing of 3.5 Å is consistent with the (040) plane of α-MoO_3. Interestingly, the annealing step in an inert atmosphere can also help the strong interface formation between C-nanopot and the heterostructure layers. Additionally, the

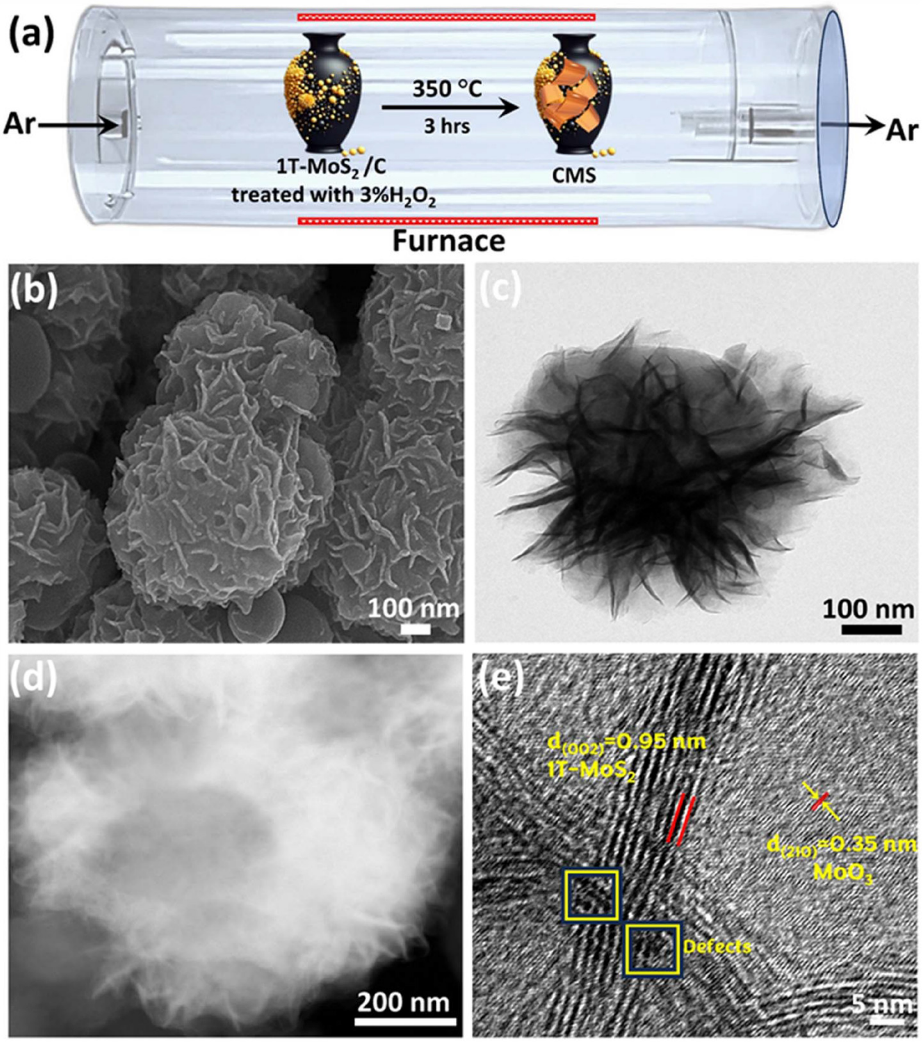

Fig. 2 (a) Scheme illustrating the synthesis of CMS; (b) SEM of CMS; (c) TEM of CMS (d) STEM of CMS; (e) HR-TEM of CMS.

relative positioning of sulfur and molybdenum atoms in the atomic layers influences the final phase of MoS_2. To comprehensively study the evidence of sulfur vacancies on CMS and the nature (chemical composition and valence states) of the interface around the designer C-nanopot, we examined the heterostructure using electron energy loss spectroscopy (EELS) and X-ray photoelectron spectroscopy (XPS) analysis. The ultrafine 2D nanosheets of the hybrid MoS_2/MoO_3 stacks over the carbon template are identified using TEM to acquire the EELS signals (Fig. 3(a) displays a TEM micrograph of the nanosheet stacks). The high-angle annular dark-field (HAADF)-STEM acquired micrograph further resolves the boundary of the interface (Fig. 3(b)), and also helps to confirm the distinct features of the boundary structure. We selected three strategic edge positions on the CMS nanostructure to acquire the EELS spectra. The carbon edge, targeting the interior carbon core, discriminates the nanostructure from its surroundings and identifies any bonding alterations near the sulfur-deficient MoS_2 region. The sulfur and molybdenum edges focus on the MoS_2 region, enabling the detection of sulfur vacancies and their impact on the local electronic structure. These edge positions optimize the spatial resolution, facilitating the precise mapping of defect-rich areas near the carbon surface. Additionally, the molybdenum and oxygen edges monitor the transformation of MoS_2 into MoO_3, characterized by changes in the Mo oxidation state and the emergence of an open, porous structure. Together, these edge selections provide clear depictions of the elemental composition, chemical shifts, and defect formation with minimal noise interference. Fig. 3(c) shows the three EELS spectra to analyse the S-$L_{2,3}$, C, and Mo-$M_{4,5}$ edges. EELS spectra were recorded in three positions marked 1, 2, and 3 in the HAADF-STEM image of the edge of a 2D stack, carbon/2D interface, and carbon surface, respectively. At region-1, the Mo–$M_{4,5}$ edge is more intense and in close proximity to the carbon surface, and the surface shows the rich sulfur vacancy with a prominence of MoO_3. In region 2, when moving away from the carbon surface and immediately to the nanosheets, the sulfur atoms exhibit diverse bonding states across the boundaries under the S-L-edge. Thus, the EELS near-edge structures for the S-$L_{2,3}$-edge and Mo-$M_{4,5}$-edge were conformably recorded.

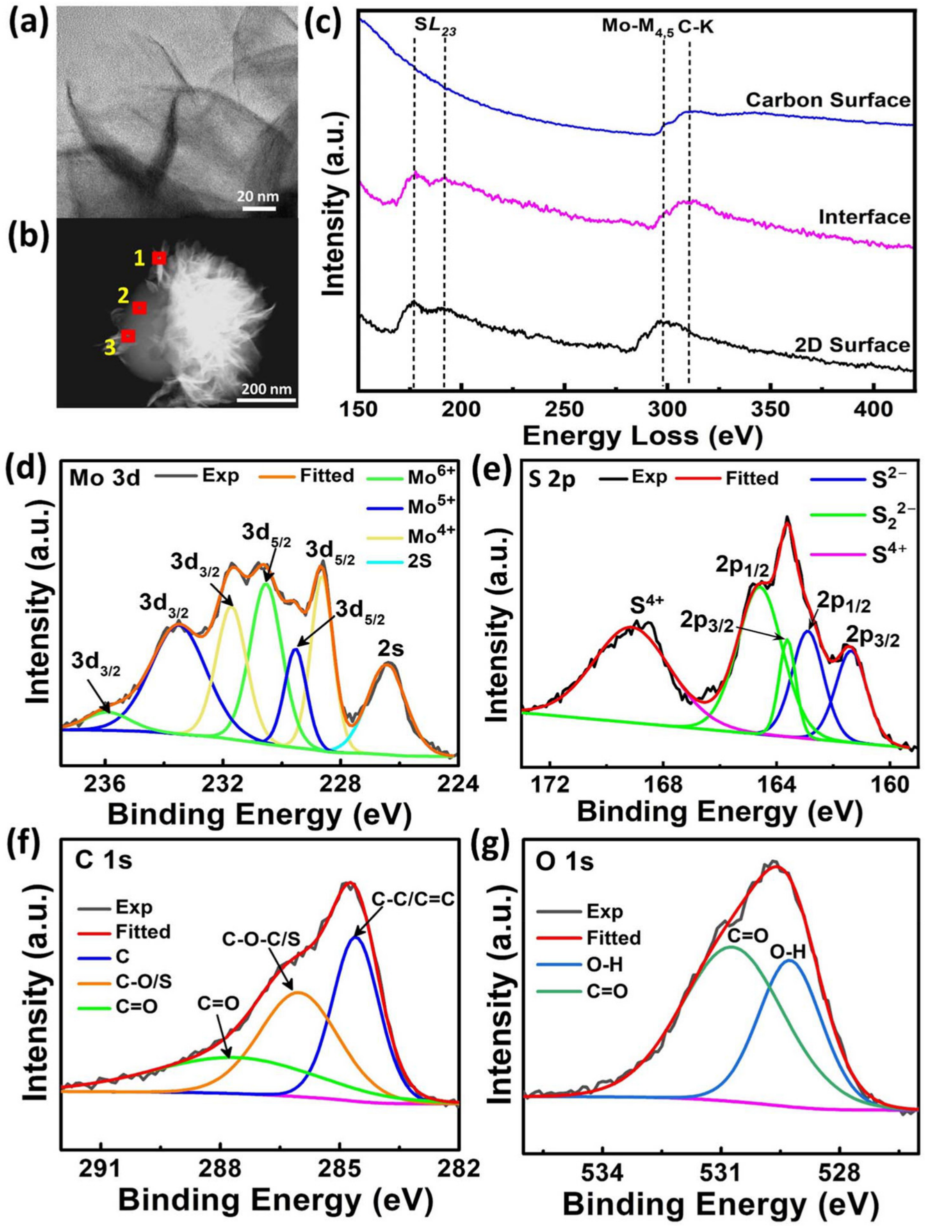

Fig. 3 (a) TEM image showing the MoS_2 layers; (b) STEM micrograph showing various EELS data acquisition points on the CMS sample marked in 1,2 and 3; (c) EELS spectra obtained on three different regions of the sample. High-resolution XPS spectra of CMS: (d) Mo 3d, (e) S 2p, (f) C 1s, and (g) O 1s.

The spectrum in region-2 shows a quantitative amount of Mo, but still confirms a substantial S deficiency. In region-3, where the MoS_2 nanosheets are vertically aligned, the S presence is relatively higher. However, a more precise quantification is often difficult as the sample thickness is not uniform, with the nanosheet's edges being radially enveloped, making the absolute quantification unfeasible. However, given the inherent metastable properties and the tendency for the phase transition of 1T-MoS_2, it is valuable to understand the composition and surface valence states of the CMS. Fig. 3(d) shows the XPS spectra of the Mo 3d orbital for the synthesized sample deconvoluted to Mo^{4+}, Mo^{5+}, and Mo^{6+} doublets, respectively. The first set of prominent peaks was observed at 228.4 ± 0.2 eV (Mo $3d_{5/2}$) and 231.8 ± 0.2 eV (Mo $3d_{3/2}$), corresponding to the 1T phase MoS_2. Conversely, the second set of doublets that emerged at 229.6 ± 0.2 eV (Mo $3d_{5/2}$) and 233.0 ± 0.2 eV (Mo $3d_{3/2}$), with an additional broad S 2p peak centered at 226.4 ± 0.2 eV,[37,38] reveals the 2H phase of MoS_2. These results reveal the co-occurrence of both the conducting (1T) and semiconducting (2H) phases of MoS_2. In addition, the doublets centered at 230.5 ± 0.2 eV and 235.9 ± 0.2 eV are ascribed to the core level of Mo $3d_{5/2}$ and $3d_{3/2}$, respectively, showing the presence of Mo^{6+} in MoO_3. Thus, the Mo doublets displayed binding energies in close proximity to its oxide configuration and exhibited a high degree of defects and sulfide deficiency. In Fig. 3(e), two spin–orbit doublets were realized from the deconvoluted S spectrum. The first set located at 161.3 ± 0.2 eV ($2p_{3/2}$) and 162.9 ± 0.2 eV ($2p_{1/2}$) correspond to apical S^{2-} ions. Another set of S doublets was also observed at 163.6 ± 0.2 eV ($2p_{3/2}$) and 164.5 ± 0.2 eV ($2p_{1/2}$), indicating the bridging $S_2{}^{2-}$ atoms.[39,40] An additional peak was also observed at 169.1 eV, which can be attributed to the S^{4+} species. Furthermore, Fig. 3(f) shows that the carbon peak can be further resolved into two main components: a prominent peak at 284.6 eV, corresponding to the C–C bonding environment (carbon scaffold), and a minor peak at 286.0 eV, assigned to the C–O bonding. This suggests that the origin of Mo–O is not from a MoO_3 phase, but rather from a Mo–O–C bonding environment at the interface between MoS_2 and carbon.[41] The O 1s region in Fig. 3(g) displays two peaks alongside the commonly observed peak at 530.0 eV allocated to Mo–O/O–H bonds. Another peak at 530.9 eV is set to C–O bonding, further corroborating the presence of Mo–O–C bonding. The occurrence of a Mo–O bond without Mo–S scission has been previously documented, suggesting a strong chemical and electronic coupling between the MoS_2 and carbon in the synthesized sample.[42] In summary, the XPS findings confirm the successful preparation of MoS_2/MoO_3 on the C-nanopots. To further supplement the information on the chemical composition, the Fourier transform infrared spectroscopy (FTIR) (provided in ESI Fig. S3†) measurement reveals essential information about the molecular components and bonding within the sample. The observed peak at 595 cm^{-1} indicates the presence of structural characteristics of MoS_2, explicitly highlighting the terminal vibration of the ν(S–S) bonds and the involvement of the bridging $S_2{}^{2-}$ ligands. The characteristic peak results from the specific molecular vibrations within the MoS_2 compound. The ν(S–S) terminal vibration involves the stretching and bending of sulfur atoms bonded to each other within individual MoS_2 units, while the bridging ligands are formed through the interaction of neighboring MoS_2 units, wherein two sulfur atoms from different units form a linkage. The peaks observed at 760 cm^{-1}, 920 cm^{-1}, and 1041 cm^{-1} suggest the formation of sulfate (SO_4) groups.[43] The absorption band at 3130 cm^{-1} (symmetric) and 3441 cm^{-1} (asymmetric stretching) represents vibrations of the O–H bond, where both oxygen and hydrogen atoms move in phase and out of phase, respectively. These peaks indicate the presence of water molecules, which may be absorbed either on the surface or within the sample. The peaks observed below 700 cm^{-1} are attributed to the (Mo–O) deformation modes,[44] and a distinct peak at 1402 cm^{-1} is due to the presence of MoS_2.[45,46] The peak at 1632 cm^{-1} indicates a C═C bond, while the peaks at 1695 cm^{-1} and 1839 cm^{-1} are attributed to C═O bonding within the molecular structure.[47] The 2846 cm^{-1} and 2925 cm^{-1} peaks represent symmetric and asymmetric (C–H) bond stretching vibration within the molecule. Another notable peak observed at 1560 cm^{-1} indicates the C═C bond and the peak at 1209 cm^{-1} confirms the existence of a C–N bond.[48]

Fig. 4(a) shows the overlay energy-dispersive X-ray spectroscopy (EDS) elementally mapped micrograph (top panel),

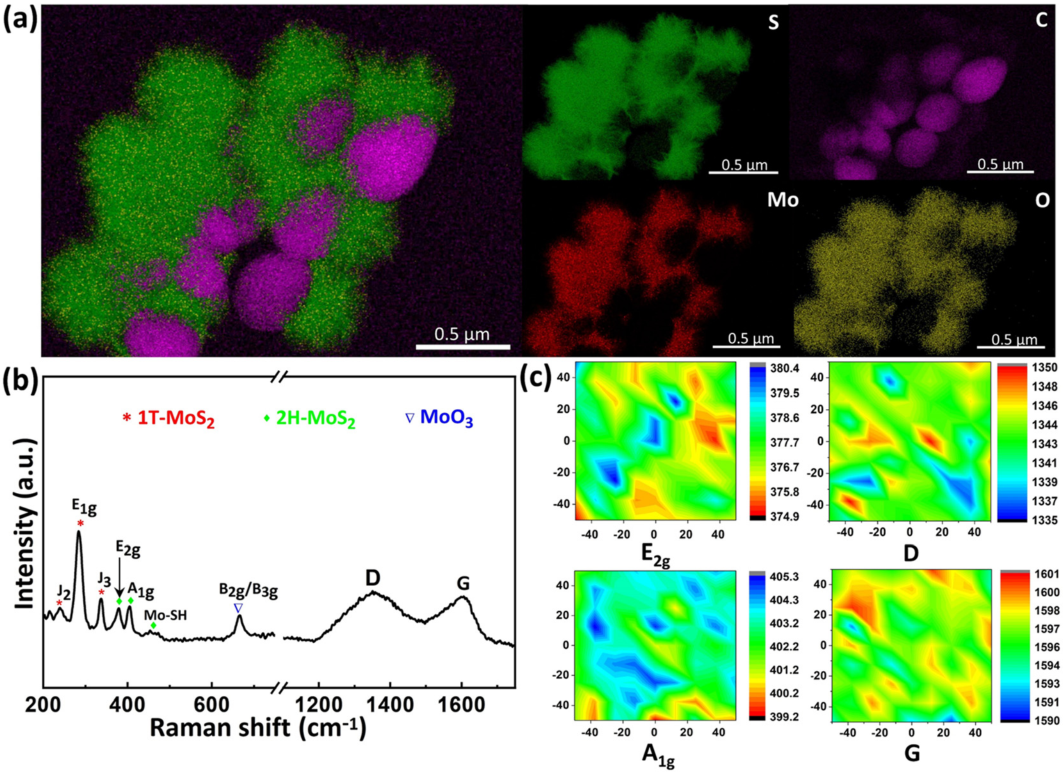

Fig. 4 (a) Elemental micrographs of the CMS sample showing the S, C, Mo, and O maps; (b) Raman spectrum of CMS; (c) Raman mapping data for MoS_2 (E_{2g} and A_{1g}) and carbon (D and G peaks) in CMS.

and also reveals the elemental distribution of the sulfur, carbon, molybdenum, and oxygen elements (right panel) in the CMS sample. From the micrographs, it is clear that both MoS_2 and MoO_3 coexist in the radially aligned nanosheets encapsulated over the carbon supports. Raman spectroscopy was utilized to understand the phase transition and molecular vibration modes of the sample, as shown in Fig. 4(b). The peak at 237 cm^{-1} (J_2) may correspond to the out-of-plane K–S Raman mode, and the 336 cm^{-1} (J_3) peak can be assigned to the stretching vibrations of the Mo–Mo bonds and phonon modes originating from the metallic 1T-MoS_2 phase (distorted tetragonal phase).[49,50] The observed peak at 283 cm^{-1} is assigned to the forbidden mode (E_{1g}), which is associated with the 1T phase.[51] Even after thermal annealing in an inert atmosphere, which improved the interface adhesion between the materials, the 1T-MoS_2 phase remained the dominant phase in the CMS. The analysis also revealed the presence of two dominant activation modes, E_{2g} (379 cm^{-1}) and A_{1g} (404 cm^{-1}), consistent with the 2H phase of MoS_2. The E_{2g} peak arises from the in-plane vibrational modes of S and Mo atoms, while the A_{1g} mode is due to the relative vibration of S atoms in the out-of-plane direction.[52,53] The peak at 450 cm^{-1} divides into three separate peaks, with frequencies of 443 cm^{-1}, 453 cm^{-1}, and 464 cm^{-1}, in ultrathin MoS_2. The presence of a prominent peak at 450 cm^{-1} in the observed spectrum is relevant to the characteristic vibrations of Mo–S bonds within the hydrosulfide (Mo–SH) species.[54,55] Interestingly, the hydrogen peak is only seen in the very thin layers of MoS_2, indicating that hydrogen mainly affects the outermost layers and not the whole material. Therefore, it's essential to recognize that the formation of these hydrosulfide complexes is likely to happen during hydrothermal reactions because there is an amine component in the precursor material. Furthermore, the Raman spectrum exhibits peaks at 665 cm^{-1}, which corresponds to the characteristics of α-MoO_3. The 665 cm^{-1} (B_{2g}/B_{3g}, asymmetric stretching) is assigned to the Mo–O–Mo bridge along the *c* axis. The resultant MoO_3 bands were consistently observed in the original MoS_2 spectrum. Thus, it is obvious that sulfur vacancies were created in MoS_2 during the thermal decomposition process. The vacant sulfur sites act as entry points for oxygen atoms, leading to the formation of MoO_3.[56] As MoO_3 forms, it can phase segregate from the remaining MoS_2, creating separate domains within the material. Thus, the presence of MoO_3 can significantly alter the electrical and catalytic properties of the material. Furthermore, CMS exhibits two wide bands at the D-band and G-band, in addition to typical peaks from 2H-MoS_2. In the amorphous carbon, the G-band corresponds to the in-plane vibrations of the sp^2-bonded carbon atoms, while the D-band originates from vibrational modes involving sp^3-bonded carbon atoms and disorder within the structure.[57] Raman mapping (Fig. 4(c)) was employed to investigate the transformation of the 1T phase to the 2H phase of MoS_2 across the carbon skeleton interface, allowing observation of the evolution of the 2H phase formation. Analysis of the E_{2g} and A_{1g} vibrational modes of 2H MoS_2 and their distribution obtained through a Gaussian profile revealed a significant red shift, potentially due to compressive strain within the MoS_2 lattice weakening the molybdenum–sulfur bonds or sulfur vacancy defects disrupting these bonds. Both factors reduce the restoring force experienced by the atoms during vibration, leading to a lower vibrational frequency (red-shift) observed in the Raman spectrum. The presence of sulfur vacancies and oxygen doping likely influences both the intralayer coupling and lattice dynamics within the MoS_2 structure. This effect may be particularly pronounced for long-range coulombic interactions between the layers. The D and G bands were also mapped to understand the peak position variations across the interfacial surface carbon. The peak shift in the G band is attributed to the stretching of the sp^2 carbon pairs within both ring and chain structures.[57] The mapped data showed a G-band position shift from 1595 cm^{-1} to 1600 cm^{-1}, explained by the inherent disorder and presence of various functionalities in the porous carbon. Furthermore, the synergistic interaction of carbon with the 2D material induced tensile strain, leading to a higher wavenumber. Finally, the D band position ranging between 1340 cm^{-1} and 1350 cm^{-1} across the mapped area indicates an abundance of defects and an amorphous character within the carbon nanopot support.

3.2 Electrochemical characterization

The electrochemical performances of the samples were tested by assembling CR2032-type coin cells. The cyclic voltammetry (CV) profiles of the CMS/S electrode in Fig. 5(a) exhibit two prominent redox peaks at 2.2 V and 1.95 V. These peaks are attributed to the multi-step conversion of sulfur to LiPSs, and ultimately to lithium sulfide (Li_2S) during the discharge process. These peaks correspond to the successive reduction of sulfur from S_8 rings to chain-like LiPSs (Li_2S_x, where $4 \le x \le 8$) and further to solid Li_2S_2/Li_2S.[58] The anodic peak observed at 2.57 V during the charging process is likely attributed to the reverse conversion of Li_2S back to LiPSs, and ultimately sulfur.[59] From Fig. 5(b), it is evident that the overpotential of the CMS/S electrode ($\Delta E \approx 290$ mV) is lower than that of the pristine C-nanopot (C/S) electrode ($\Delta E \approx 370$ mV) during the stable discharge cycle. This confirms that the uniform distribution of sulfur is achieved and enhances the redox reaction kinetics of LiPS during the galvanostatic charge–discharge (GCD) process, with an augmented specific capacity of ~1270 mA h g^{-1} compared to the counterpart with a specific capacity of 708 mA h g^{-1} at 0.2 A g^{-1}. The enhanced performance of CMS can be attributed to the synergetic effects of defect-rich MoS_2 confined to the MoO_3 matrix and carbon nanopots. Hybridizing with carbonaceous materials improved the interfacial binding strength between the carbon nanopots and the 2D layers. The poor electrical conductivities of sulfur and MoO_3 were also effectively alleviated. The sulfur host provides higher ionic conductivity for fast Li^+ charge transfer and allows effective chemical adsorption of polysulfides for the conversion to Li_2S_2/Li_2S. Fig. 5(c) illustrates the plots of the diffusion coefficient values (D_{Li^+}) from the electrochemical impedance spectroscopy (EIS) profiles to investigate the effects

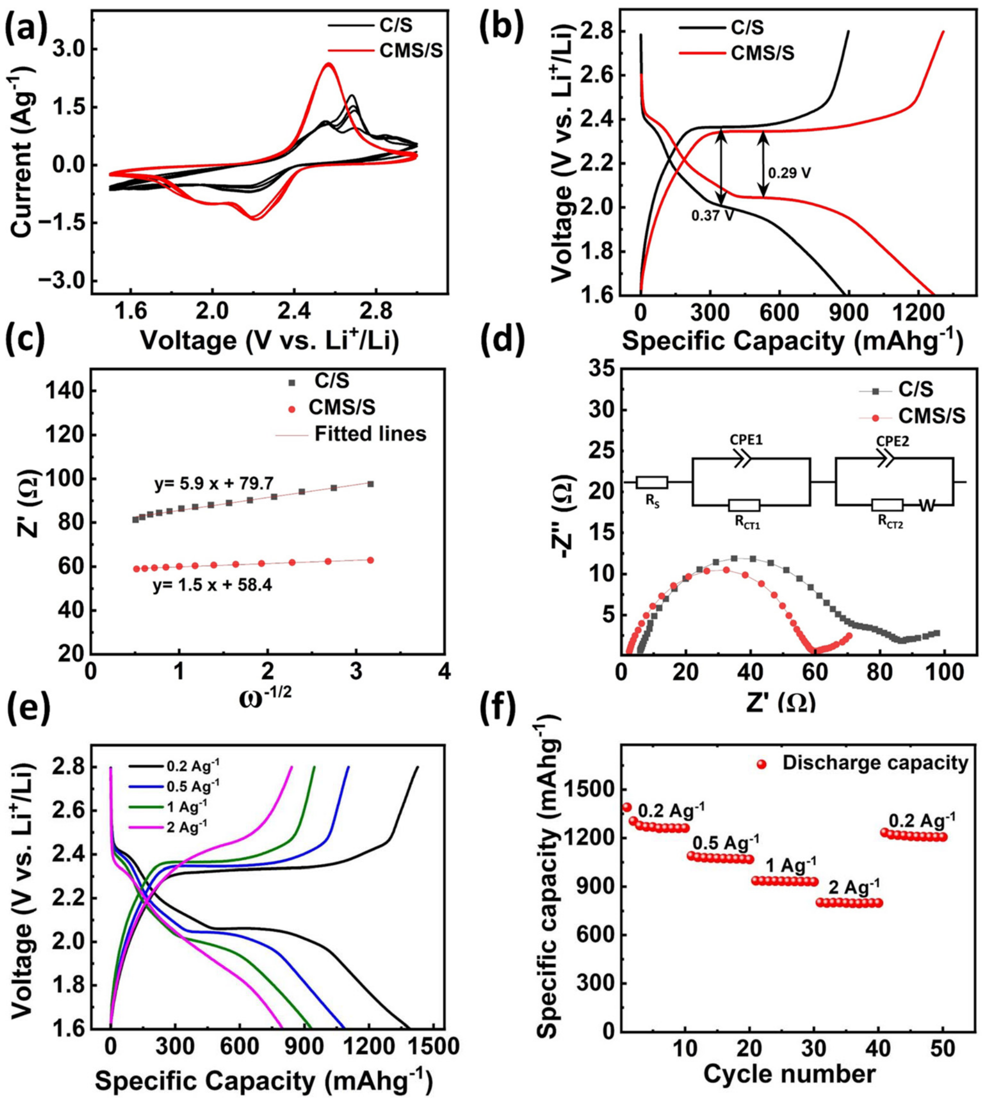

Fig. 5 (a) Comparison of the cyclic voltammetric response of C/S and CMS/S. (b) Comparative galvanostatic charge–discharge profiles. (c) Warburg slopes determination from the Z' *vs.* $\omega^{-1/2}$ plot; (d) EIS plot. (e) Initial specific capacities of CMS/S obtained at various current densities. (f) Rate capability of the CMS/S obtained from 0.2 A g^{-1} to 2 A g^{-1}.

of active material, which reflects the transport properties under dynamic conditions,

$$\text{Diffusion coefficient } (D) = \frac{1}{2}(RT/An^2F^2C\sigma)^2$$

The equation takes into account various factors to calculate the rate at which lithium ions move within the electrode material during charge and discharge. These factors include the universal gas constant (R = 8.314 J K^{-1} mol^{-1}), temperature (T, typically set at room temperature, 298 K), the number of electrons transferred in the specific electrochemical reaction (n), a constant that converts between the number of electrons and the amount of material involved (Faraday constant, F = 96 485 C mol^{-1}), the estimated concentration of lithium ions stored per unit volume in the electrode (C, measured in mol cm^{-3}), the actual physical area of the electrode (A, typically around 1.5 cm^2), and a factor related to the inherent speed of the reaction within the material (pre-exponential factor or Warburg factor, σ). By considering these parameters, the equation allows researchers to analyse and potentially improve the performance of batteries. The Warburg factor is obtained from the slopes of Z' *vs.* $\omega^{-1/2}$

$$Z' = \sigma\omega^{-1/2} - j\sigma\omega^{-1/2}$$

All electrodes exhibit the Warburg-type diffusion response, characterized by the ∼45° line in the low-frequency region of the Nyquist plots (Fig. 5(c)), indicating a linear trend of Z' *vs.* $\omega^{-1/2}$ with a constant slope (σ) within experimental error. This suggests sluggish diffusion kinetics in C/S, which is likely due to insoluble short-order polysulfides. Conversely, the presence of a favorable electrode structure in the CMS/S, where sulfur or long-order LiPSs are well-integrated within the support and porous carbon nanotemplates, leads to enhanced diffusion coefficients (1.48×10^{-8} cm^2 s^{-1}) compared to C/S (3.75×10^{-9} cm^2 s^{-1}). The sluggish reaction kinetics in the pristine sample is further evidenced by the high ohmic overpotential. This is likely mitigated in the CMS based cathode by the creation of S vacancies, which, along with the highly active and large surface area MoS_2 nanosheets grown radially on carbon templates, may compensate for both reaction and concentration overpotentials. In this work, the hollow carbon nanopots function as a LiPS reservoir, preventing their diffusion away from the electrode. Notably, the CMS/S maintains uniform and high LiPS concentrations within the nanopots during conversion, facilitating mass diffusion and fast conversion efficiency. Additionally, MoS_2/MoO_3 nanosheets reduce the LiPS diffusion distance and minimize the impact of the concentration gradients. The unique combination of factors embodied by the CMS nanostructure facilitates the simultaneous trapping and efficient electrocatalytic conversion of LiPS. Fig. 5(d) displays the EIS spectra of the C/S and CMS/S electrodes. An equivalent circuit model is also provided as an inset in Fig. 5(d). From the EIS analysis, the high-frequency intercept on the real axis (Z') corresponds to the electrolyte resistance (R_s). At medium frequencies, the observed semicircle represents the combination of two phenomena: charge transfer resistance (R_{ct}) and interfacial capacitance. The latter is often denoted by a constant phase element (CPE) to account for non-idealities. At low frequencies, the Warburg impedance (W_0) manifests as a sloped line, indicating the diffusion of Li^+ within the electrode. The sulfur-loaded CMS electrode (CMS/S) exhibits a significantly lower R_{ct} (57.37 Ω) compared to sulfur-loaded C-nanopot (C/S) with a value of (80.5 Ω). This significant decrease signifies a facilitated charge transfer process in the electrode due to the interaction between MoS_2 and the porous carbon nanostructure. The porous nature of the carbon likely provides enhanced pathways for electrolyte penetration and ion diffusion, while MoO_3/MoS_2 may act as a catalyst for redox reactions. It is possible that the Mo–O bond in α-MoO_3 enables strong polarity towards efficient LiPS trapping.[60] This aligns with the observed faster redox kinetics from EIS analysis. From the GCD analysis obtained at various current densities, it is observed that the CMS/S electrode exhibits the highest initial capacity of ~1392 mA h g^{-1} at 0. 2 A g^{-1} (Fig. 5(e)). The rate performances of the CMS/S electrode (Fig. 5(f)) demonstrated its ability to accelerate redox conversion during the Li–S battery charge–discharge processes. The rate capability test evaluated from 0.2 to 2 A g^{-1} reveals that the CMS/S discharge capacity stabilizes at 1263 mA h g^{-1} after 10 cycles at 0.2 A g^{-1}. Notably, the CMS/S maintains a stable coulombic efficiency at all current densities, indicating optimal sulfur utilization. When the discharge rate returns to 0.2 A g^{-1}, the specific capacity recovers to 1205 mA h g^{-1}, demonstrating excellent rate performance. The conversion capability of Li_2S_n to Li_2S and *vice versa* (bidirectional liquid–solid conversion) heavily relies on the electrode material's ability to adsorb and catalytically convert these species.

A schematic illustration involving the bifunctional mechanism of the CMS/S electrode is presented in Fig. 6(a). The synergistic mechanism of carbon nanopots encapsulated with MoS_2/MoO_3 structures serves three purposes. The physical confinement of LiPS in the carbon nanopot's pores and cavities prevents them from shuttling throughout the cell. The chemical adsorption of 2D heterostructure's active sites with strong chemical bonds that attract and hold LiPS, further inhibiting their movement.

Finally, the heterostructure can also accelerate the conversion of LiPS back to sulfur during charging, minimizing the dead sulfur proportion in the electrode. The enhancement in diffusion coefficients also confirms the argument. To further validate the strong adsorption capability/catalytic conversion activity of the CMS nanostructure for polysulfides, a visual adsorption test was conducted. In a controlled experiment (Fig. 6(b)-inset), equal quantities of the C-nanopot and CMS materials were incorporated into a Li_2S_6 solution within an inert atmosphere glove box. A blank solution and Super-P carbon were included as controls. Over time, the yellow color of the Li_2S_6 solution containing CMS faded completely, signifying a superior and more rapid adsorption capability of CMS compared to the other materials. The C-nanopots partially removed the yellow color, while Super-P exhibited minimal adsorption. This adsorption test confirms that CMS possesses the strongest adsorption and catalytic activity for polysulfides in a Li_2S_6 solution. The UV visible absorption spectra (Fig. 6(b)) suggest a potent chemical interaction between CMS and Li_2S_6, providing clear evidence for the decrease in the polysulfide concentration. The characteristic peaks corresponding to S_6^{2-}/S_4^{2-} exhibit decreased intensity in the spectra of C-nanopot and CMS. The intensity prominently disappears in the spectrum of the CMS heterostructure. These results demonstrate that the polysulfide absorptivity of the heterostructure is significantly higher than that of pristine C-nanopots. This enhanced absorptivity is attributed to the formation of a conductive network by MoS_2, which facilitates sulfur redox reactions, improving electrode stability and sulfur utilization, thereby boosting the battery performance. Additionally, MoO_3, acting as a strong adsorbent, prevents polysulfide dissolution and mitigates the polysulfide shuttle effect, a major cause of capacity fading in lithium–sulfur batteries. Together, MoS_2 and MoO_3 catalyze the conversion of soluble polysulfides into insoluble Li_2S/Li_2S_2, improving the cycling stability. MoS_2's strong affinity for polysulfides, combined with MoO_3's adsorption capacity, limits polysulfide dissolution and promotes efficient S_8 ring breakdown into Li_2S_2, further reducing the shuttle effect and enhancing the overall battery performance.[61]

Fig. 6(c) highlights the superior specific capacity retention of CMS/S compared to that of C/S. At a low current density of 0.2 A g^{-1}, CMS/S retains ~89% specific capacity, while the C/S material exhibited ~70% capacity retention over 200 cycles. The cycle life trend in CMS/S is driven by the interaction between the 1T-MoS_2/MoO_3 heterostructure, carbon nanopot, and sulfur species. Initially, the CMS/S cathode shows stable

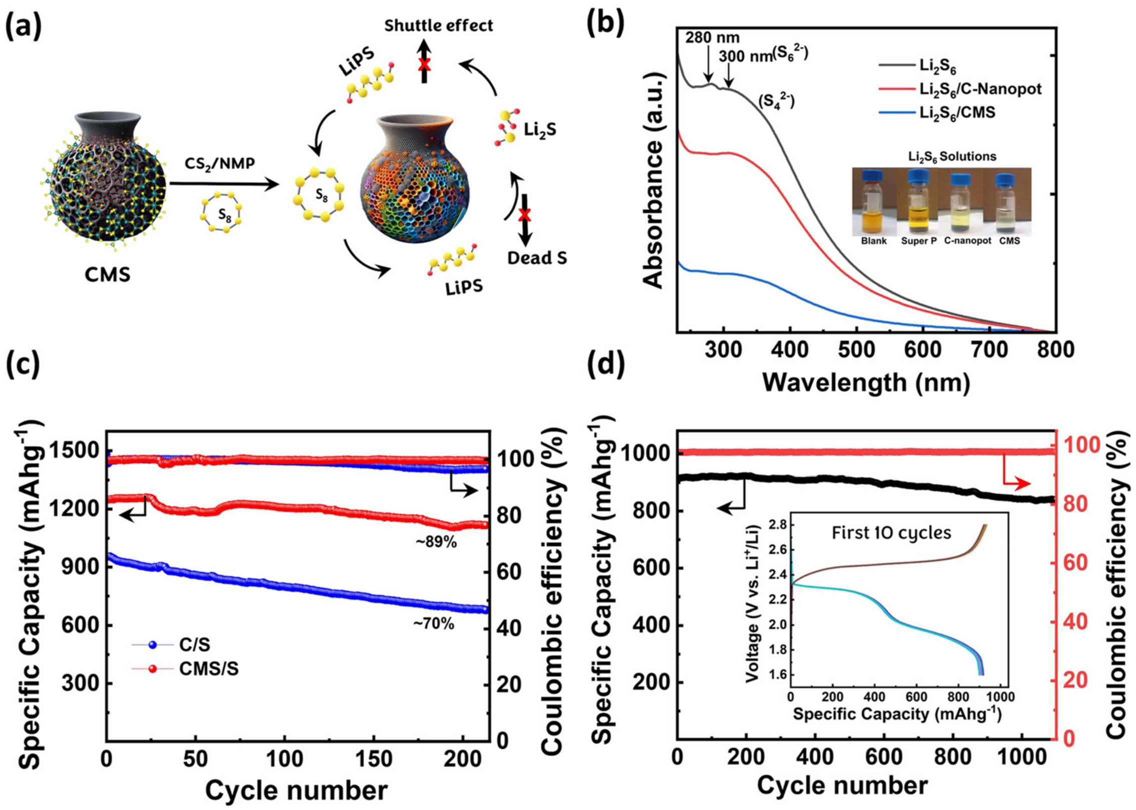

Fig. 6 (a) Sulfur-loaded CMS (CMS/S) sample showing the mechanism of electrocatalytic conversion of polysulfides. (b) Polysulfide adsorption test and UV visible spectra of a polysulfides-saturated samples. (c) Specific capacity retention and coulombic efficiencies of the C/S and CMS/S electrodes obtained at a low current density of 0.2 A g^{-1}. (d) Cyclic stability and coulombic efficiency of CMS/S at 1 A g^{-1} (inset shows initial ten charge–discharge cycles).

capacity, reflecting the efficient sulfur conversion to Li_2S during discharge and sulfur regeneration during charge. After 25 cycles, a slight capacity decline occurs due to the polysulfide shuttle effect, where dissolved polysulfides migrate to the anode, react with lithium, and cause capacity loss. However, cycle life stabilizes as improved polysulfide trapping and sulfur utilization occur. Structural changes in the CMS/S cathode and enhanced conductivity of the carbon support boost polysulfide adsorption and sulfur interaction, leading to stable performance. The significant enhancement is also attributed to the catalytic conversion of adsorbed polysulfides back to sulfur at the interface.[62,63]

In comparison to recent advances, Ma *et al.* utilized the catalytic effects of a CNT/MoS_2–Co nanocomposite cathode to suppress lithium polysulfide dissolution, achieving a capacity decay of 0.050% per cycle over 1000 cycles at 5C.[64] Similarly, a dual-function molecular catalyst combining sulfur with $[Mo_2S_{12}]^{2-}$ demonstrated a capacity decay of 0.065% over 600 cycles at 3C.[65] Ni *et al.* employed a polyoxometalate-cyclodextrin cluster-organic supramolecular framework (Zn_2W_2@2CD)-modified separator to mitigate the polysulfide shuttle, resulting in a capacity decay of 0.064% per cycle over 500 cycles at 1C.[66]

As shown in Fig. 6(d), the CMS/S electrode exhibits exceptional long-term cycling performance, delivering a stable specific capacity of 834 mA h g^{-1} at a high current density of 1 A g^{-1}, with a capacity decay of only 0.078% over 1100 cycles. This confirms that CMS acts as an efficient catalytic host material with excellent reversibility. With ~90% retention of its initial capacity and ~99% coulombic efficiency, the symmetrical charge–discharge profile (Fig. 6(d)-inset) further underscores the robust redox kinetics maintained over prolonged cycling.

This high performance highlights the effectiveness of CMS/S in promoting efficient charge transport and sulfur utilization, positioning CMS/S as a highly promising solution for achieving stable, long-lasting Li–S batteries, surpassing or matching many state-of-the-art approaches in terms of both cycle stability and capacity retention.

4. Conclusion

To address the challenges of Li–S batteries, a synergistic electrode design has been developed. This design combines high surface area carbon nanopots as sulfur hosts encapsulated with a defect-rich MoS_2/MoO_3 heterostructure. The hybrid structure offers a dual role for capturing and converting lithium polysulfides (LiPS) during discharge. The heterostructure provides strong binding sites for LiPS, and facilitates their conversion back to usable lithium sulfide (Li_2S) during charge. Furthermore, enhanced conductivity is achieved through both the carbon pots and the 1T-MoS_2 phase within the heterostructure. MoO_3 plays a multifunctional role, offering additional reaction sites, maintaining structural integrity during cycling, promoting electron transport, and faster Li-ion diffusion rate ($D_{Li^+} = 1.48 \times 10^{-8}$ cm^2 s^{-1}) for CMS/S. These features resulted in a stable reversible capacity of 1106 mA h g^{-1} at 0.2 A g^{-1} over 200 cycles and 834 mA h g^{-1} at 1 A g^{-1}, respectively, even after 1100 charge–discharge cycles. This emphasizes CMS as a potential material for various electrocatalytic and battery applications.

Author contributions

Sakthivel Kaliyaperumal: conceptualization, methodology, data curation, investigation, writing – original draft. Karthik Kiran Sarigamala: conceptualization, investigation, formal analysis, validation, resources, project administration, supervision, writing – review & editing. Padmini Moorthy: investigation, data curation, formal analysis, writing – review & editing. Balaji Ramachandran: formal analysis, validation. Narendhar Chandrasekar: formal analysis, validation. Tim Albrecht: writing – review & editing.

Data availability

Data supporting this article have been included as part of the ESI.†

Conflicts of interest

There are no conflicts to declare.

Acknowledgements

The authors would like to acknowledge support from the Sponsored Research and Industrial Consultancy (SpoRIC) SEED GRANT (RGEMS) VIT Vellore (SPL/SG20230142).

References

1 A. Thakur and B. Anasori, *Science*, 2024, **383**(6688), 1182–1183.

2 H. Zhang, *ACS Nano*, 2015, **9**(10), 9451–9469.

3 X. Chen, Y.-J. Park, M. Kang, S.-K. Kang, J. Koo, S.-M. Shinde, J. Shin, S. Jeon, G. Park, Y. Yan, M.-R. MacEwan, W.-Z. Ray, K.-M. Lee, J.-A. Rogers and J.-H. Ahn, *Nat. Commun.*, 2018, **9**(1), 1690.

4 Z. Wang and B. Mi, *Environ. Sci. Technol.*, 2017, **51**(15), 8229–8244.

5 S. H. Choi, S. J. Yun, Y. S. Won, C. S. Oh, S. M. Kim, K. K. Kim and Y. H. Lee, *Nat. Commun.*, 2022, **13**(1), 1484.

6 S. Liang, B. Cheng, X. Cui and F. Miao, *Adv. Mater.*, 2020, **32**(27), 1903800.

7 A. D. Handoko, K. D. Fredrickson, B. Anasori, K. W. Convey, L. R. Johnson, Y. Gogotsi, A. Vojvodic and Z. W. Seh, *ACS Appl. Energy Mater.*, 2018, **1**(1), 173–180.

8 K. K. Sarigamala, A. Struck, S. Shukla and S. Saxena, *Electrochim. Acta*, 2023, **450**, 142266.

9 S. Park, A. T. Garcia-Esparza, H. Abroshan, B. Abraham, J. Vinson, A. Gallo, D. Nordlund, J. Park, T. R. Kim, L. Vallez, R. Alonso-Mori, D. Sokaras and X. Zheng, *Adv. Sci.*, 2021, **8**(9), 2002768.

10 N. Lopez-Pinto, T. Tom, J. Bertomeu, J. M. Asensi, E. Ros, P. Ortega and C. Voz, *Appl. Surf. Sci.*, 2021, **563**, 150285.

11 T. Y. Ko, A. Jeong, W. Kim, J. Lee, Y. Kim, J. E. Lee, G. H. Ryu, K. Park, D. Kim, Z. Lee, M. H. Lee, C. Lee and S. Ryu, *2D Mater.*, 2016, **4**(1), 014003.

12 K. K. Sarigamala, S. Shukla and S. Saxena, *Mater. Today Energy*, 2024, **44**, 101627.

13 A. A. Bortoti, A. de F. Gavanski, Y. R. Velazquez, A. Galli and E. G. de Castro, *J. Solid State Chem.*, 2017, **252**, 111–118.

14 P. E. Sheehan and C. M. Lieber, *Science*, 1996, **272**(5265), 1158–1161.

15 A. Yoon, J. H. Kim, J. Yoon, Y. Lee and Z. Lee, *ACS Appl. Mater. Interfaces*, 2020, **12**(19), 22029–22036.

16 B. A. Holler, K. Crowley, M. Berger and X. P. A. Gao, *Adv. Electron. Mater.*, 2020, **6**(10), 2000635.

17 M. C. Lemme, D. Akinwande, C. Huyghebaert and C. Stampfer, *Nat. Commun.*, 2022, **13**(1), 1392.

18 W. Jan, A. D. Khan, F. J. Iftikhar and G. Ali, *J. Energy Storage*, 2023, **72**, 108559.

19 L. Yu, S. J. H. Ong, X. Liu, D. Mandler and Z. J. Xu, *Electrochim. Acta*, 2021, **392**, 139013.

20 D. Lei, W. Shang, X. Zhang, Y. Li, S. Qiao, Y. Zhong, X. Deng, X. Shi, Q. Zhang, C. Hao, X. Song and F. Zhang, *ACS Nano*, 2021, **15**(12), 20478–20488.

21 J. Yang, Y. Qu, X. Lin, L. Wang, Z. Zheng, J. Zhuang and L. Duan, *Electrochim. Acta*, 2022, **418**, 140378.

22 Y. Song, L. Shen, N. Yao, S. Feng, Q. Cheng, J. Ma, X. Chen, B. Li and Q. Zhang, *Angew. Chem., Int. Ed.*, 2024, **63**, e202400343.

23 Y.-W. Song, L. Shen, N. Yao, X.-Y. Li, C.-X. Bi, Z. Li, M.-Y. Zhou, X.-Q. Zhang, X. Chen, B.-Q. Li, J.-Q. Huang and Q. Zhang, *Chem*, 2022, **8**, 3031–3050.

24 M. Zhao, H.-J. Peng, B.-Q. Li and J.-Q. Huang, *Acc. Chem. Res.*, 2024, **57**(4), 545–557.

25 Q. Cheng, Z.-X. Chen, X.-Y. Li, L.-P. Hou, C.-X. Bi, X.-Q. Zhang, J.-Q. Huang and B.-Q. Li, *J. Energy Chem.*, 2023, **76**, 181–186.

26 X. Ji, K. T. Lee and L. F. Nazar, *Nat. Mater.*, 2009, **8**, 500–506.

27 D. Wang, G. Du, Y. Wang, Y. Fan, D. Han, Q. Su, S. Ding, W. Zhao, M. Zhang and B. Xu, *J. Colloid Interface Sci.*, 2023, **630**, 535–543.

28 M. Li, H. Peng, Y. Pei, F. Wang, Y. Zhu, R. Shi, X. He, Z. Lei, Z. Liu and J. Sun, *Nanoscale*, 2020, **12**(46), 23636–23644.

29 J. Hu, Y. Xie, X. Zhou and Z. Zhang, *ACS Appl. Mater. Interfaces*, 2020, **12**(1), 1232–1240.

30 B. Wang, Y. Xia, J. Bai, G. Yuan and H. Ma, *J. Alloys Compd.*, 2024, **970**, 172617.

31 Q. Shao, P. Lu, L. Xu, D. Guo, J. Gao, Z.-S. Wu and J. Chen, *J. Energy Chem.*, 2020, **51**, 262–271.

32 Y. Huang, L. Lin, C. Zhang, L. Liu, Y. Li, Z. Qiao, J. Lin, Q. Wei, L. Wang, Q. Xie and D. Peng, *Adv. Sci.*, 2022, **9**(12), 2106004.

33 C. Zhang, Z. Wang, S. Bhoyate, T. Morey, B. Neria, V. Vasiraju, G. Gupta, S. Palchoudhury, P. Kahol, S. Mishra, F. Perez and R. Gupta, *C*, 2017, **3**(4), 33.

34 K. Chang, W. Chen, L. Ma, H. Li, H. Li, F. Huang, Z. Xu, Q. Zhang and J.-Y. Lee, *J. Mater. Chem.*, 2011, **21**(17), 6251.

35 Q. Liu, X. Li, Q. He, A. Khalil, D. Liu, T. Xiang, X. Wu and L. Song, *Small*, 2015, **11**, 5556–5564.

36 H. Fan, R. Wu, H. Liu, X. Yang, Y. Sun and C. Chen, *J. Mater. Sci.*, 2018, **53**, 10302–10312.

37 J. Tang, J. Huang, D. Ding, S. Zhang and X. Deng, *Int. J. Hydrogen Energy*, 2022, **47**(94), 39771–39795.

38 M. Acerce, D. Voiry and M. Chhowalla, *Nat. Nanotechnol.*, 2015, **10**(4), 313–318.

39 Y. Hu and D. H. C. Chua, *Sci. Rep.*, 2016, **6**(1), 28088.

40 X. Zi, J. Wan, X. Yang, W. Tian, H. Zhang and Y. Wang, *Appl. Catal., B*, 2021, **286**, 119870.

41 N. Zeng, D. G. Hopkinson, B. F. Spencer, S. G. McAdams, A. A. Tedstone, S. J. Haigh and D. J. Lewis, *Chem. Commun.*, 2019, **55**(1), 99–102.

42 H. Long, A. Harley-Trochimczyk, T. Pham, Z. Tang, T. Shi, A. Zettl, C. Carraro, M. A. Worsley and R. Maboudian, *Adv. Funct. Mater.*, 2016, **26**(28), 5158–5165.

43 G. A. M. Ali, M. R. Thalji, W. C. Soh, H. Algarni and K. F. Chong, *J. Solid State Electrochem.*, 2020, **24**(1), 25–34.

44 A. S. Krishna Kumar, S.-J. Jiang and J. K. Warchol, *ACS Omega*, 2017, **2**(9), 6187–6200.

45 K. C. Lalithambika, K. Shanmugapriya and S. Sriram, *Appl. Phys. A*, 2019, **125**(12), 817.

46 M. Yi and C. Zhang, *RSC Adv.*, 2018, **8**(17), 9564–9573.

47 W. Feng, L. Chen, M. Qin, X. Zhou, Q. Zhang, Y. Miao, K. Qiu, Y. Zhang and C. He, *Sci. Rep.*, 2015, **5**(1), 17422.

48 B. Chen, H. Lu, J. Zhou, C. Ye, C. Shi, N. Zhao and S. Qiao, *Adv. Energy Mater.*, 2018, **8**(15), 34–39.

49 H. S. S. Ramakrishna Matte, A. Gomathi, A. K. Manna, D. J. Late, R. Datta, S. K. Pati and C. N. R. Rao, *Angew. Chem., Int. Ed.*, 2010, **49**(24), 4059–4062.

50 S. Jiménez Sandoval, D. Yang, R. F. Frindt and J. C. Irwin, *Phys. Rev. B: Condens. Matter Mater. Phys.*, 1991, **44**(8), 3955–3962.

51 H. Li, X. Yuan, Z. Wei, J. Shi, Q. Jia, D. Ma, Y. Li, Y. Zhang and X. Zhu, *Mater. Today Chem.*, 2024, **37**, 102002.

52 I. Song, C. Park and H. C. Choi, *RSC Adv.*, 2015, **5**(10), 7495–7514.

53 Z. Luo, J. Li, Y. Li, D. Wu, L. Zhang, X. Ren, C. He, Q. Zhang, M. Gu and X. Sun, *Adv. Energy Mater.*, 2022, **12**(12), 2103823.

54 H. Li, Q. Zhang, C. C. R. Yap, B. K. Tay, T. H. T. Edwin, A. Olivier and D. Baillargeat, *Adv. Funct. Mater.*, 2012, **22**(7), 1385–1390.

55 E. Payen, S. Kasztelan, S. Houssenbay, R. Szymanski and J. Grimblot, *J. Phys. Chem.*, 1989, **93**(17), 6501–6506.

56 R. Szoszkiewicz, *Phys. Chem. Chem. Phys.*, 2023, **25**(18), 12555–12564.

57 A. C. Ferrari and J. Robertson, *Phys. Rev. B*, 2000, **61**(20), 14095–14107.

58 T. Hou, W. Xu, X. Chen, H. Peng, J. Huang and Q. Zhang, *Angew. Chem., Int. Ed.*, 2017, **56**(28), 8178–8182.

59 H. Ye, J. Sun, S. Zhang, H. Lin, T. Zhang, Q. Yao and J. Y. Lee, *ACS Nano*, 2019, **13**(12), 14208–14216.

60 H. Dai, L. Wang, Y. Zhao, J. Xue, R. Zhou, C. Yu, J. An, J. Zhou, Q. Chen, G. Sun and W. Huang, *Research*, 2021, **2021**, 5130420.

61 J. Yang, Y. Qu, X. Lin, L. Wang, Z. Zheng, J. Zhuang and L. Duan, *Electrochim. Acta*, 2022, **418**, 140378.

62 M. Wang, H. Yang, K. Shen, H. Xu, W. Wang, Z. Yang, L. Zhang, J. Chen, Y. Huang, M. Chen, D. Mitlin and X. Li, *Small Methods*, 2020, **4**(9), 2000353.

63 W. Li, D. Wang, Z. Song, Z. Gong, X. Guo, J. Liu, Z. Zhang and G. Li, *Nano Res.*, 2019, **12**, 2908–2917.

64 Z. Ma, Y. Liu, J. Gautam, W. Liu, A. N. Chishti, J. Gu, G. Yang, Z. Wu, J. Xie, M. Chen, L. Ni and G. Diao, *Small*, 2021, **17**(39), 2102710.

65 Z. Ma, W. Liu, X. Jiang, Y. Liu, G. Yang, Z. Wu, Q. Zhou, M. Chen, J. Xie, L. Ni and G. Diao, *ACS Nano*, 2022, **16**, 14569–14581.

66 L. Ni, J. Gu, X. Jiang, H. Xu, Z. Wu, Y. Wu, Y. Liu, J. Xie, Y. Wei and G. Diao, *Angew. Chem., Int. Ed.*, 2023, **62**(36), e202306528.